Article

Seismic Design and Performance Evaluation of Coupled Steel Plate and Reinforced Concrete Composite Walls

Aozhou Liu [1], Yuntian Wu [2,*], Bin Wang [1] and Xiyue Chen [1]

1   School of Civil Engineering, Chongqing University, Chongqing 400045, China
2   Department of Civil and Environmental Engineering, University of Houston, Houston, TX 77204, USA
*   Correspondence: ywu77@uh.edu

Abstract: Coupled steel plate and reinforced concrete (SPRC) composite shear walls have been widely constructed in the core tube of super tall buildings in seismic regions. However, relevant research progress is far behind the practical application of this coupled composite wall system. Particularly, the current seismic design method does not consider the coupling mechanism and lacks efficiency in the computation of seismic base shear. In this research, the energy balance-based plastic design (EBPD) method is developed and used to design twelve prototype structures considering different structural heights and coupling ratios (CR). With the ABAQUS-based numerical techniques verified by relevant experimental results, all the prototype cases were studied by pushover analysis and nonlinear dynamic analysis to examine the effectiveness of the EBPD method in ensuring satisfactory seismic performance of coupled SPRC composite walls. The results indicate that the coupled SPRC composite walls designed by the EBPD method can satisfy the code requirements on lateral deformation under moderate and rare earthquakes. The analytical average story shear and bending moment distribution patterns have acceptable agreement with the relevant design assumptions. Favorable CR ranges are suggested for the coupled SPRC composite walls with different story numbers to achieve good earthquake-induced deformation characteristics.

Keywords: steel plate; composite shear wall; coupled wall; energy balance; plastic design; coupling ratio

1. Introduction

Coupled steel plate and reinforced concrete (SPRC) composite walls are commonly used in the core tube of super tall buildings. Architecturally, the core tube walls with large openings at each story provide space, support and a gateway to the vertical transportation system of the super tall buildings. Structurally, the wall openings are large enough to divide the core tube walls into separate piers joined only by steel coupling beams (SCB) at floor levels, thereby forming the coupled wall system. For the bottom stories and basement of super tall buildings, the axial load demand transferred from the upper stories is extremely high, with the result that it is very difficult to satisfy the axial load ratio limitation. By embedding steel plates in the middle of the concrete wall, the SPRC composite section can achieve a stable high strength in axial and shear resistance with a reasonable thickness. Figure 1 shows a construction site with coupled SPRC composite walls of a super tall building. However, in practical design, the characteristics of the coupling mechanism are ignored; mainly the composite action of the SPRC walls is considered in calculating the axial load capacity. Although coupled SPRC composite walls have been widely constructed, their benefits and advantages over conventional isolated composite walls have not been satisfactorily utilized because current codes do not differentiate between coupled and non-coupled composite walls [1].
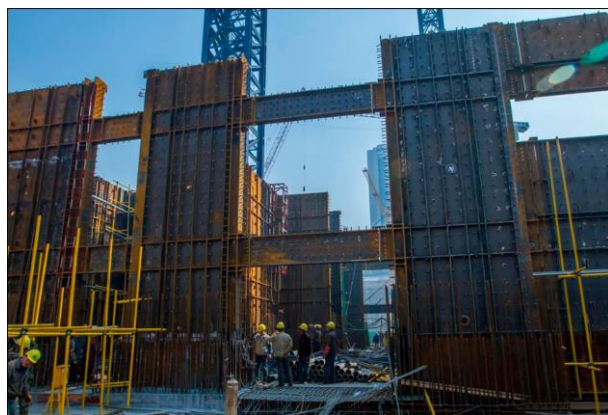
Figure 1. Construction site of coupled SPRC composite walls.

Previous research on coupled SPRC composite walls has been limited, largely due to the difficulty and cost of experimental studies. In the reported tests on the subassembly models consisting of one-and-a-half stories of SPRC walls and a half-span of SCB, the test subassemblies were subjected to horizontal reversed cyclic loads applied to the top of the SPRC walls to evaluate the responses of the SCBs and the SPRC wall piers [2,3]. These subassembly test results demonstrated the high performance of the test models with the fully developed coupling mechanism. The influences of the key design parameters and construction details on the overall behavior of the coupled SPRC composite walls were also revealed. Another reported test on a 1:4 scale five-story coupled SPRC composite wall system focused on the plasticity development and distribution pattern determined by the coupling mechanism [4]. The test results indicated that the coupled composite system can be designed to dissipate energy primarily by the shear deformation of the SCBs and the plastic hinge deformation at the bottom of the SPRC wall. It is worth mentioning that another type of coupled composite wall system has also been tested, where the test model was a 1:5 scale five-story core tube containing a steel truss instead of steel plate-reinforced concrete wall piers joined by reinforced concrete or steel-reinforced concrete coupling beams [5]. The test results showed that the embedded steel trusses significantly affect the seismic performance of the coupled composite core walls in terms of lateral load carrying capacity, energy dissipation and damage mode.

It can be seen that although only limited experimental studies have been conducted, the excellent overall seismic performance of the coupled SPRC composite walls has been validated. Further research is needed to develop systematic and efficient seismic design method for coupled SPRC composite wall systems. In this research, the energy balance-based plastic design (EBPD) method is introduced and used for the seismic design of the coupled SPRC composite system. The EBPD method is based on the energy balance concept, which suggests that the input earthquake energy is equal to the sum of the damping energy and cumulative plastic work [6]. This energy balance-based design method was first introduced to the design of steel moment frames. The advantage of the energy concept was demonstrated by directly calculating the base shear from the energy balance equation without further iteration [7]. The plastic limit analysis was then used in accordance with the pre-selected yielding pattern and the target ultimate lateral drift of the structural system [8]. It was indicated that the seismic design results from the EBPD method became more controllable than those from conventional seismic design methods. The EBPD method has been applied to the seismic design of various structural systems, including steel concentric braced frames [9], hybrid coupled walls [10], buckling-restrained braced non-ductile RC frames [11] and composite partially restrained steel frame-reinforced concrete infill walls with concealed vertical slits [12]. The EBPD method was further improved by introducing an energy reduction factor to take into account the accumulated damage and the pinching effect of concrete structures [13,14].

In this research, the EBPD method is developed for the seismic design of coupled SPRC composite walls. In order to examine the seismic performance of the coupled SPRC walls designed by the EBPD method, 12 prototype cases with different structural heights and coupling ratios (CR) were designed and studied. A series of pushover analyses and nonlinear dynamic time history analyses were conducted to examine the performance characteristics of the coupled SPRC composite walls designed using the EBPD method.

2. EBPD Method for Coupled SPRC Composite Walls

2.1. Energy Balance Equation

The energy balance equation of a structural system subjected to earthquake ground motions is expressed by Equation (1):

$$E_e + \eta E_p = \gamma E_I \tag{1}$$

where E_e and E_p are the elastic and plastic energy developed in the structural system; E_I is the total input earthquake-induced energy; η is the energy reduction factor; and γ is the energy modification factor. In order to calculate the total input earthquake energy E_I, the structural system is assumed to be an elastic multi-degree-of-freedom (E-MDOF) system, where m_i and k_i are the concentrated mass and the lateral stiffness of the ith story. The E-MDOF system can be further decomposed into multiple modes of elastic single-degree-of-freedom (E-SDOF) systems. The ith mode E-SDOF system can be defined by M_i and K_i, or the ith modal mass and stiffness. The EI can be computed by Equation (2):

$$E_I = \sum_{i=1}^{N} \frac{1}{2} M_i^* S_{v,i}^2 = \sum_{i=1}^{N} \frac{1}{2} M_i^* \left(\frac{S_{a,i} T_i}{2} \right)^2 \tag{2}$$

where N is the total story number of the structure; and $S_{v,i}$, M_i^*, $S_{a,i}$ and T_i are the pseudo velocity, the effective modal mass, the pseudo acceleration and the period corresponding to the ith mode E-SDOF system. $S_{a,i}$ can be determined using the design response spectrum given in the Chinese code [15]. The energy modification factor γ can be obtained by Equation (3):

$$\gamma = \frac{2\mu - 1}{R_\mu^2} \tag{3}$$

where μ is the displacement ductility factor; and R_μ is the ductility reduction factor. It is obvious that γ is introduced to account for the difference between the energy that an inelastic and an elastic structural system can absorb.

The elastic energy stored in the structure, E_e, is the elastic vibrational energy that is gradually released as the vibrational velocity reduces.

$$E_e = \frac{1}{2} V_y \Delta_y = \frac{1}{2} M \left(\frac{T_1}{2\pi} \cdot \frac{V_y}{G} \cdot g \right)^2 \tag{4}$$

where M and G are the total mass and the seismic weight of the structure; V_y and Δ_y are the design base shear and the corresponding roof lateral displacement; and T_1 is the elastic fundamental period of the structure.

As shown in Figure 2, the plastic energy E_p is associated with the design base shear V_y and can be computed as the work performed by the design base shear V_y after the yielding of the structure.

$$E_p = \sum_{i=1}^{N} F_i h_i \theta_p = V_y \theta_p \sum_{i=1}^{N} \lambda_i h_i \tag{5}$$

where F_i is the lateral load applied to the ith floor; h_i is the height measured from the ground to the ith floor level; and θ_p is the plastic rotation, or the difference between the target ultimate lateral drift ratio, θ_u, and the inter-story-drift ratio at yielding, θ_y, which can be 1/250, as suggested by Park et al. [16].
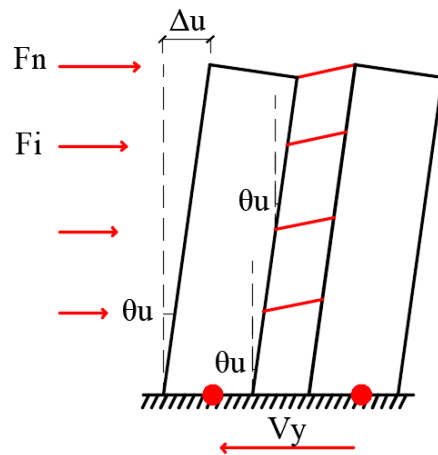
Figure 2. Ideal ultimate yielding condition.

According to previous research [17], the lateral force at the ith floor F_i can be computed by Equations (6) and (7):

$$F_i = \lambda_i V_y = (\beta_i - \beta_{i+1}) \left(\frac{G_n h_n}{\sum_{j=1}^{N} G_j h_j} \right)^{0.75 T_1^{-0.2}} V_y \tag{6}$$

$$\beta_i = \frac{V_i}{V_n} = \left(\sum_{j=i}^{N} G_j h_j / G_n h_n \right)^{0.75 T_1^{-0.2}} \tag{7}$$

where λ_i is the lateral force distribution factor for the ith floor; G_n and G_j, and h_n and h_j are the seismic weight concentrated at the roof and the jth floor, and the structural height measured from ground to the roof and the jth level, respectively; V_i and V_n are the story shears of the ith story and the top story; and β_i is the story shear distribution factor for the ith story.

The hysteretic energy modification factor η is used to account for the area reduction of the ideal load versus displacement hysteretic loops due to stiffness degradation, strength deterioration, and pinching effects of concrete structures. The formulas in Table 1 can be used to estimate the value of η corresponding to different hysteretic models. It is suggested that the small Takeda model is suitable for coupled SPRC composite walls [12].

Table 1. Hysteretic energy modification factor η.

Model	Ring-Spring	Large Takeda	Small Takeda
$T_{\text{eff}} < 1$ s	$\frac{0.3 + 0.35(1-T_{\text{eff}})}{0.85 + 0.6(1-T_{\text{eff}})}$	$\frac{0.65 + 0.5(1-T_{\text{eff}})}{0.85 + 0.6(1-T_{\text{eff}})}$	$\frac{0.5 + 0.4(1-T_{\text{eff}})}{0.85 + 0.6(1-T_{\text{eff}})}$
$T_{\text{eff}} \geq 1$ s	0.353	0.765	0.588

In Table 1, T_{eff} is the equivalent fundamental period of the structure and can be calculated by:

$$T_{\text{eff}} = T_1 \sqrt{\mu / (1 + \alpha \mu - \alpha)} \tag{8}$$

where α is the ratio of the initial stiffness to that after yielding; and μ is the displacement ductility ratio. Combining Equations (2), (4) and (7) into Equation (1), the design base shear can be obtained.

$$V_y = \frac{-\eta \theta_p \sum_{i=1}^{N} \lambda_i h_i + \sqrt{\left(\eta \theta_p \sum_{i=1}^{N} \lambda_i h_i \right)^2 - 4 \cdot (2T_e^2/8\pi^2 M) \cdot \left(-\gamma \sum_{i=1}^{N} \frac{1}{2} M_i^* S_{v,i}^2 \right)}}{2T_1^2/8\pi^2 M} \tag{9}$$

The lateral force at each floor can be calculated by Equation (10) with the consideration of the additional lateral force ΔF_i caused by the *P-Δ* effect.

$$F_i = \lambda_i V_y + \Delta F_i = \lambda_i V_y + G_i \theta_u \tag{10}$$

Then the total overturning moment M_{otm} can be determined by Equation (11).

$$M_{otm} = \sum_{i=1}^{N} F_i h_i \tag{11}$$

2.2. Plastic Design of Coupled SPRC Composite Walls

The coupling ratio is defined as the ratio of the moment due to the coupling effect to the total overturning moment.

$$CR = \frac{Tl_w}{Tl_w + M_{cw} + M_{tw}} \tag{12}$$

where T is the sum of the axial tension force transferred from coupling beams to an SPRC wall pier; l_w is the centroidal distance between the two adjacent SPRC wall piers; and M_{cw} and M_{tw} are the overturning moments carried by the wall piers on the compression side and the tension side, respectively. Based on the pre-selected CR value and the total overturning moment, the total shear demand of the coupling beams is given by:

$$T = \sum_{i=1}^{N} V_{bi} = \frac{M_{otm} \cdot CR}{l_w} \tag{13}$$

where V_{bi} is the shear demand of coupling beam at the *i*th floor. The shear demand distribution among the coupling beams at different floors can be determined by Equation (14).

$$V_{bi} = \frac{\beta_i}{\sum_{i=1}^{N} \beta_i} \cdot \sum_{i=1}^{N} V_{bi} \tag{14}$$

As shown in Figure 3, the shear capacity of the SCBs (red line) can be adjusted by up to 20% of the maximum of the shear demand (black line) to allow the redistribution of shear forces among SCBs on different floors [18]. The shear forces transferred from the SCBs to the adjacent walls are amplified by a factor of 1.11 due to the overstrength of the SCBs [19].
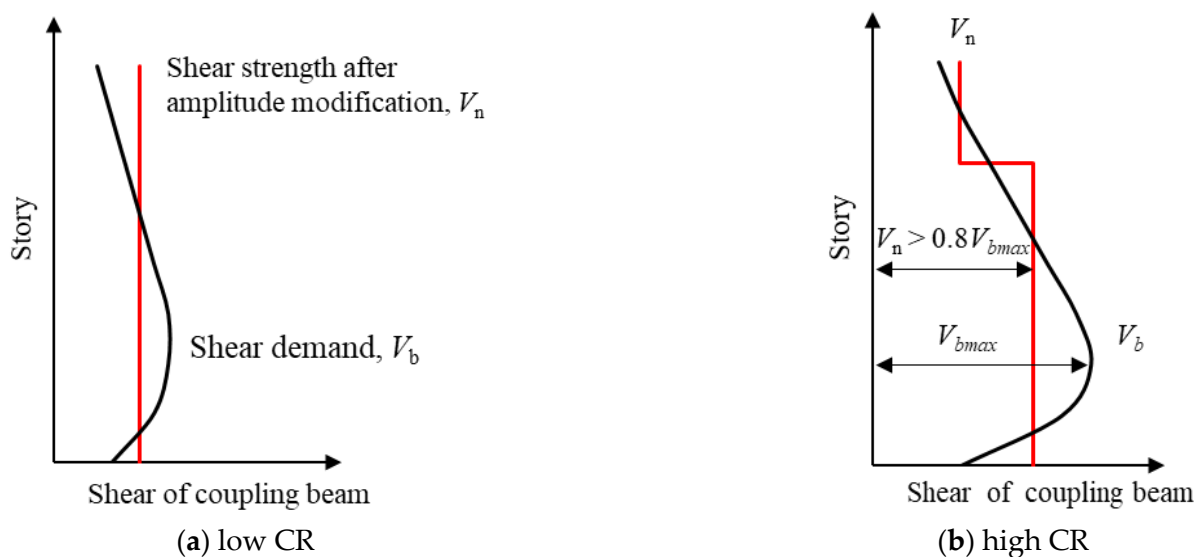

Figure 3. Redistribution of shear demands of SCBs.

The overturning moment carried by the wall piers, M_w, is the sum of the moments resisted by the wall on the compression side, M_{cw}, and that on the tension side, M_{tw}, and can be calculated by Equation (15).

$$M_w = M_{cw} + M_{tw} = M_{otm}\cdot(1 - CR) \tag{15}$$

However, the overturning moments resisted by the wall piers are not evenly distributed. Table 2 lists the distribution proportions between the compression and tension piers corresponding to different CRs.

Table 2. Proportions of bending moment distribution (%).

Wall Pier	CR			
	0.3	0.4	0.5	0.6
Compression pier	0.55	0.58	0.61	0.64
Tension pier	0.45	0.42	0.39	0.36

3. Prototype Coupled SPRC Composite Walls

Based on the proposed EBPD method, a total of 12 prototype cases of the coupled SPRC composite wall were designed in accordance with the Chinese codes [15,20], considering three structural heights of 12, 16, 20 stories and four coupling ratios of 30%, 40%, 50% and 60%. The design peak ground acceleration (PGA) was 0.4 g. The 12 prototype structures were divided into three groups, each group containing four prototype cases with the same story number. Then different coupling ratios were assigned to the four cases of each group. The prototype case is identified by the story number and CR. For example, the identification C-12-30 represents a 12-story coupled SPRC composite wall structure with a CR of 30%. All the prototype cases have the same overall dimensions. The length and story height of the wall pier are 4000 mm and 3000 mm, respectively. The clear span length of the SCBs is 2000 mm. The wall thicknesses for the C-12, C-16 and C-20 groups of prototype cases are 200 mm, 250 mm and 300 mm, respectively. The nominal compressive strength of the concrete is 40 MPa, while the nominal steel yield strength is 400 MPa for the longitudinal and transverse reinforcements. The nominal yield strength of the steel for the SCBs, the embedded steel columns at boundary elements and the steel plates is 345 MPa. The thicknesses of the steel plates embedded in the wall piers for the C-12, C-16 and C-20 groups are 5 mm, 6 mm and 7 mm respectively. The cross-sections of the SCBs and the embedded steel columns at the boundary elements of the SPRC wall piers for the C-12 group prototype cases are given in Tables 3 and 4.

Table 3. Cross-section dimensions of SCBs ($d \times b_f \times t_w \times t_f$) for C-12 group (Unit: mm).

ID	2nd–4th Stories	5th–7th Stories	8th–10th Stories	11th Floor–Roof
C-12-30	410 × 200 × 8 × 30	410 × 200 × 7.5 × 30	410 × 200 × 6.5 × 30	240 × 200 × 6 × 20
C-12-40	460 × 200 × 9.5 × 30	460 × 200 × 9 × 30	460 × 200 × 7.5 × 30	340 × 200 × 6 × 20
C-12-50	570 × 200 × 10 × 35	570 × 200 × 9 × 35	560 × 200 × 7.5 × 30	400 × 200 × 6 × 20
C-12-60	580 × 200 × 12 × 40	570 × 200 × 11 × 35	560 × 200 × 9 × 30	400 × 200 × 7 × 25

The C-12 group prototype cases are used as the example to show the design results of the SPRC composite walls. The stirrup reinforcement at the boundary elements of the wall piers of all the 12 prototype structures consists of #12 rebars at a spacing of 100 mm. The uniformly distributed reinforcement of the wall piers in both horizontal and vertical directions consists of #12 rebars at a spacing of 200 mm. The longitudinal reinforcement at the boundary elements of the wall piers is shown in Table 5.

Table 4. Embedded steel column ($d \times b_f \times t_w \times t_f$) of wall piers for C-12 group (Unit: mm).

ID	1st Story	2nd Story	3rd–8th Stories	9th–12th Stories
C-12-30	$400 \times 160 \times 5 \times 15$	$400 \times 160 \times 5 \times 12$	$400 \times 160 \times 8 \times 15$	$400 \times 160 \times 8 \times 15$
ID	**1st–2nd Stories**	**3rd Story**	**4th–8th Stories**	**9th–12th Stories**
C-12-40	$400 \times 160 \times 5 \times 12$	$400 \times 160 \times 8 \times 15$	$400 \times 160 \times 5 \times 12$	$400 \times 160 \times 5 \times 12$
C-12-50	$400 \times 160 \times 5 \times 12$	$400 \times 160 \times 5 \times 12$	$400 \times 160 \times 5 \times 12$	$400 \times 160 \times 5 \times 12$
C-12-60	$400 \times 160 \times 5 \times 12$	$400 \times 160 \times 5 \times 12$	$400 \times 160 \times 5 \times 12$	$400 \times 160 \times 5 \times 12$

Table 5. Longitudinal reinforcement at boundary elements for C-12 group.

ID	1st Story	2nd Story	3rd–4th Stories	5th Story	6th–12th Stories
C-12-30	8#32	8#28	8#32	8#25	8#18
C-12-40	8#32	8#25	8#32	8#22	8#18
ID	**1st Story**	**2nd Story**	**3rd Story**	**4th Story**	**5th–12th Stories**
C-12-50	8#25	8#18	8#32	8#28	8#18
C-12-60	8#20	8#18	8#28	8#25	8#18

4. Finite Element (FE) Modeling and Verification

4.1. Concrete Modeling

Numerical models of the 12 prototype structures were established using ABAQUS. The concrete damage plasticity (CDP) model is adopted to simulate concrete. The stress–strain relationship of concrete in the CDP model is shown in Figure 4. The initial elasticity modulus E_0 can be calculated using the compressive strain $\varepsilon_{c,e0}$ and stress $\sigma_{c,e0}$ corresponding to the elastic limit by Equation (16). $\sigma_{c,e0}$ can be taken as one-third of the concrete compressive strength f_c. The cracking strain in the tensile stage $\varepsilon_{t,in}$ and the inelastic strain in the compression stage $\varepsilon_{c,in}$ can be computed by Equations (17) and (18).

$$E_0 = \frac{\sigma_{c,e0}}{\varepsilon_{c,e0}} \tag{16}$$

$$\varepsilon_{t,in} = \varepsilon_t - \varepsilon_{c,in}\sigma_t / E_0 \tag{17}$$

$$\varepsilon_{c,in} = \varepsilon_c - \sigma_c / E_0 \tag{18}$$

where σ_t is the stress at any point at the hardening stage of tension; ε_t is the corresponding strain; and ε_c and σ_c are the strain and stress during the hardening stage of compression.

The tensile and compressive damage variables D_t and D_c are introduced to account for the stiffness degradation of concrete caused by damage during the stress–strain hysteretic process. The expressions of the uniaxial tensile and compressive stress–strain relationship of the concrete can be given by Equations (19) and (20). Inserting Equations (17) and (18) into Equations (19) and (20), the tension plastic strain, $\varepsilon_{t,p}$, and the compression strain, $\varepsilon_{c,p}$, can be calculated by Equations (21) and (22)

$$\sigma_t = (1 - D_t)E_0(\varepsilon_t - \varepsilon_{t,p})\sigma_c \tag{19}$$

$$\sigma_c = (1 - D_c)E_0(\varepsilon_c - \varepsilon_{c,p}) \tag{20}$$

$$\varepsilon_{t,p} = \varepsilon_{t,in} - \frac{D_t}{1 - D_t}\frac{\sigma_t}{E_0} \tag{21}$$

$$\varepsilon_{c,p} = \varepsilon_{c,in} - \frac{D_c}{1 - D_c}\frac{\sigma_c}{E_0} \tag{22}$$

Other basic parameters in the CDP model are summarized in Table 6. f_{b0}/f_{c0} is the ratio of the biaxial compressive strength to the uniaxial compressive strength. K is the ratio of the second stress invariant on the tensile meridian to that on the compressive meridian.
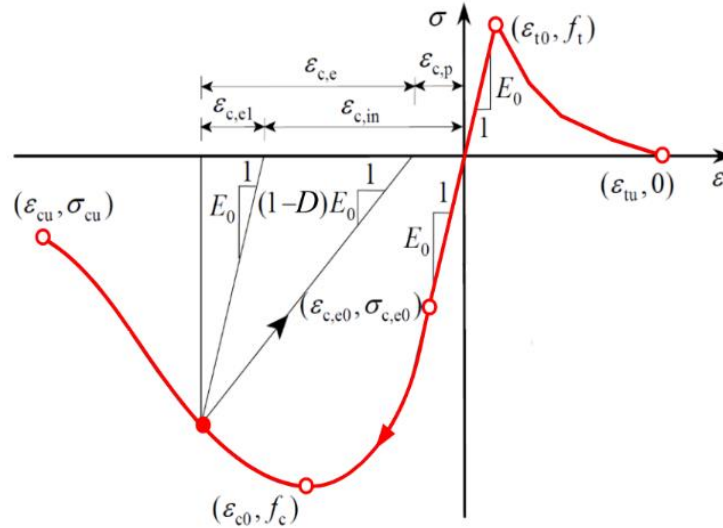

Figure 4. Stress–strain curve of concrete.

Table 6. Parameter values in the CDP model.

Dilation Angle	Flow Potential Eccentricity	f_{b0}/f_{c0}	K	Viscosity Coefficient	Concrete Poisson's Ratio
38°	0.1	1.16	2/3	0.001	0.2

4.2. Reinforcement Modeling

The Usteel02 model in ABAQUS is adopted to simulate the reinforcing bars with consideration of the loading phase, yield plateau, unloading phase and failure of the reinforcement. The corresponding stress–strain curve of the Usteel02 model in the PQ-fiber subprogram is depicted in Figure 5.
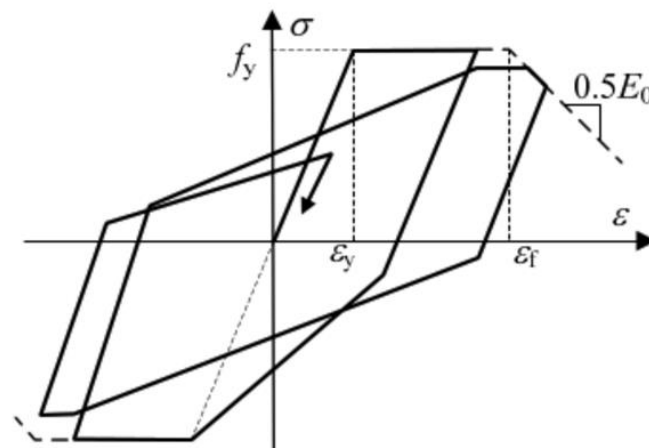
Figure 5. Stress–strain curves of USteel02 of PQ-fiber.

4.3. Structural Steel Modeling

The modeling of the structural steel material for the steel members follows the constitutive relationship provided in the Eurocode [21] and used in previous research [22,23], which is indicated by Equation (23) and Figure 6.

$$\sigma = \begin{cases} \varepsilon E_s & \varepsilon \leq \varepsilon_p \\ f_y & \varepsilon_p \leq \varepsilon \leq \varepsilon_y \\ f_y + \frac{f_u - f_y}{\varepsilon_s - \varepsilon_y}\left(\varepsilon - \varepsilon_y\right) & \varepsilon_y \leq \varepsilon \leq \varepsilon_s \\ f_u & \varepsilon_s \leq \varepsilon \leq \varepsilon_t \\ f_u\left(1 - \frac{\varepsilon - \varepsilon_t}{\varepsilon_u - \varepsilon_t}\right) & \varepsilon_t \leq \varepsilon \leq \varepsilon_u \\ 0 & \varepsilon > \varepsilon_u \end{cases} \tag{23}$$

where σ is the stress of the steel; f_u is the ultimate tensile stress of the steel; ε_p is the proportional limit strain of the steel; ε_s is the ultimate strength strain of the steel; and ε_t is the strength degradation strain of the steel.
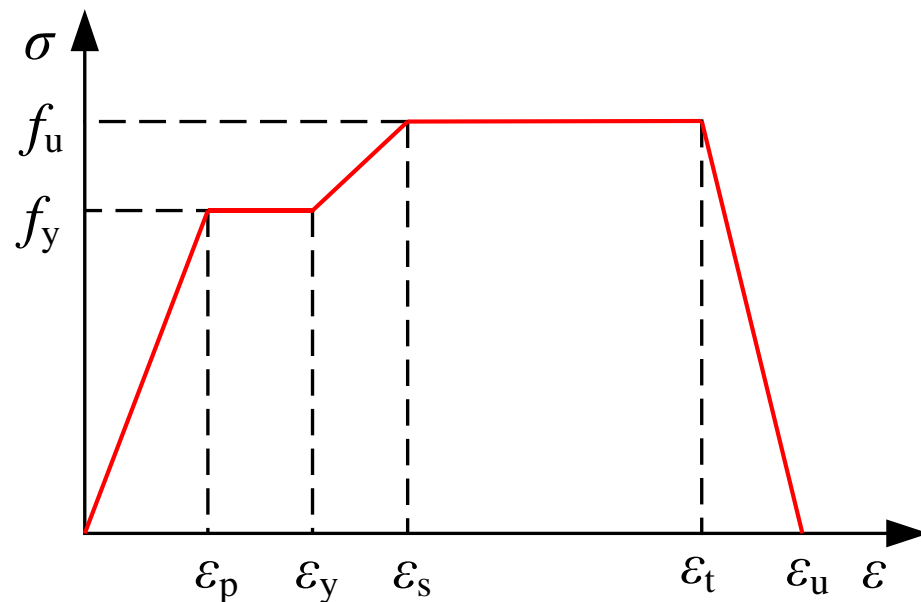
Figure 6. Constitutive model of steel.

4.4. FE Types and Mesh Size

In the numerical simulation, a three-dimensional solid eight-node hexahedral element C3D8R is used for concrete. The truss element T3D2 is used for reinforcement, which can only bear axial loads. The reduced integral curved shell element S4R with four nodes is used for steel members. In order to obtain accurate and computationally cost-effective simulation, the reinforcement and steel members of all 12 prototype cases adopt a mesh size of 200 mm. Concrete meshing sizes of 200 mm, 250 mm and 300 mm are used for the C-12, C-16 and C-20 groups of prototype cases, respectively.

4.5. Verification of Modeling Techniques

To verify the accuracy of the above-mentioned numerical modeling techniques, the 1:4 scale five-story coupled SPRC composite wall specimen [4] was modeled and analyzed. Then the numerically simulated results were compared with the experimental ones. The experimental and simulated results are compared in Figure 7, which shows the lateral force versus displacement hysteretic loops and skeleton curves.
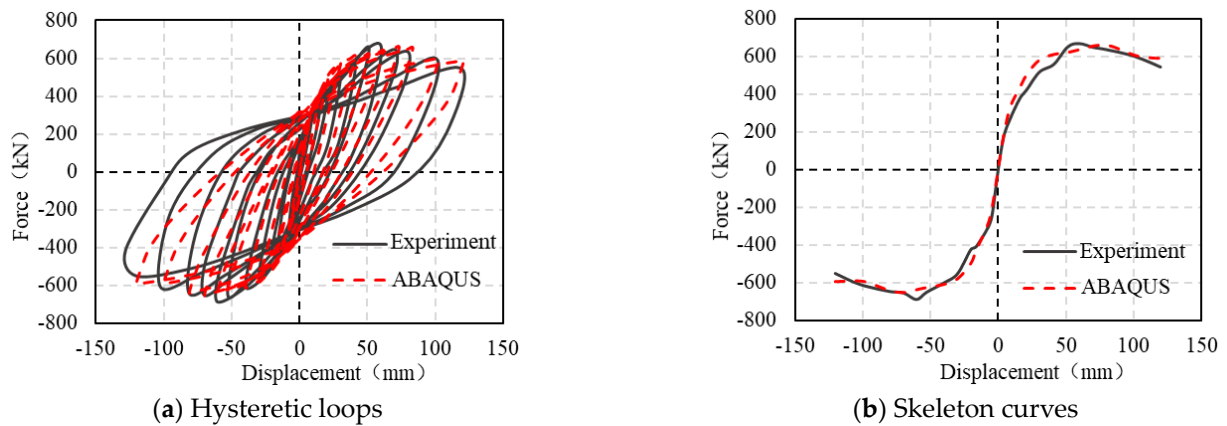
(**a**) Hysteretic loops

(**b**) Skeleton curves

Figure 7. Comparison of experimental and numerical results.

5. Pushover Analysis

A pushover analysis on the 12 prototype cases of the coupled SPRC wall structures was conducted to obtain the capacity curves. The lateral force distribution pattern proposed by Chao et al. was adopted [18].

5.1. Capacity Curves

The capacity curves of the 12 prototype cases are shown in Figure 8. On each capacity curve the circle, square and triangle marks indicate the yielding of 50% of the SCBs, the yielding of the bottom region of the wall pier and the yielding of longitudinal reinforcement or steel members at the upper region of the wall pier, respectively. It can be seen that the capacity curves of the three prototype groups demonstrate very similar characteristics. The yielding of 50% of SCBs manifests the yielding of the entire structural system with a significant reduction in the lateral stiffness, followed by yielding of the bottom region of the wall piers. The yielding of the upper region of the wall piers occurs when the capacity curves are close to the peak lateral load capacity. Within each prototype group, the smaller the CR, the smaller the roof lateral drift ratio corresponding to the yielding of 50% of the SCBs. However, the roof lateral drift ratios corresponding to the yielding of the bottom region and upper region of the wall piers increase. This means using a smaller CR can result in better post-yield deformation capacity. On the other hand, the larger the CR, the greater the lateral load capacity.

(**a**) 12-story

(**b**) 16-story

Figure 8. *Cont.*

(**c**) 20-story
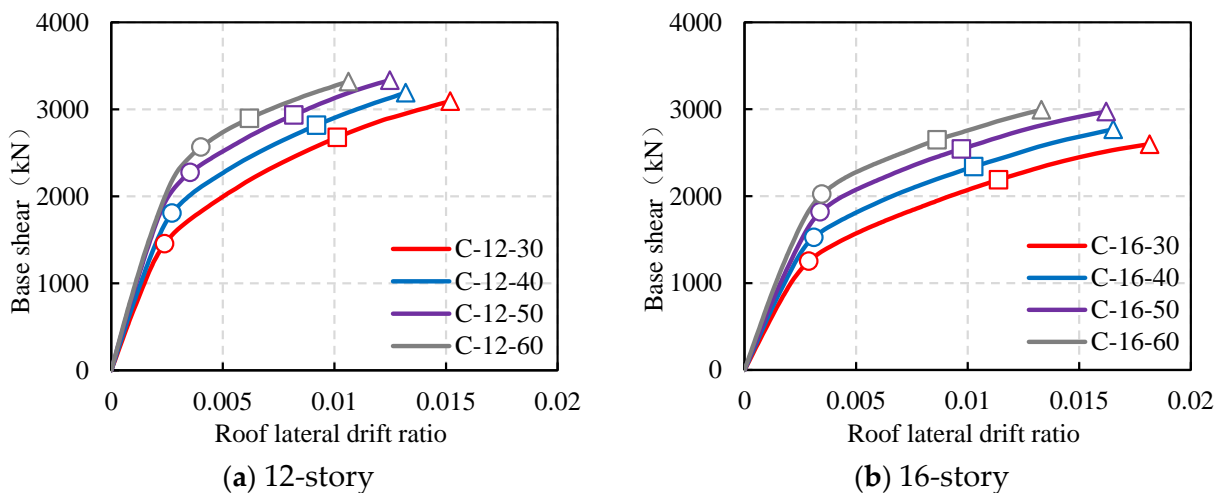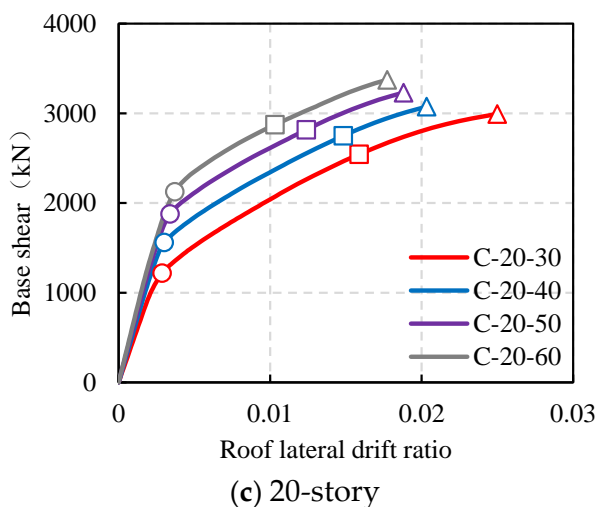
Figure 8. Capacity curves of all prototype structures.

Figure 9 shows the maximum inter-story drift ratio of the 12 prototype structures corresponding to the characteristic events. As can be seen in Figure 9a, when 50% of SCBs yield, the maximum inter-story drift ratios of all prototype cases do not exceed 1/120. When the bottom sections of the wall piers yield, almost all prototype cases have developed maximum inter-story drift ratios between 1/120 and 1/80, as shown in Figure 9b.

(**a**) Yielding of 50% of all SCBs

(**b**) Yielding of wall pier bottom section
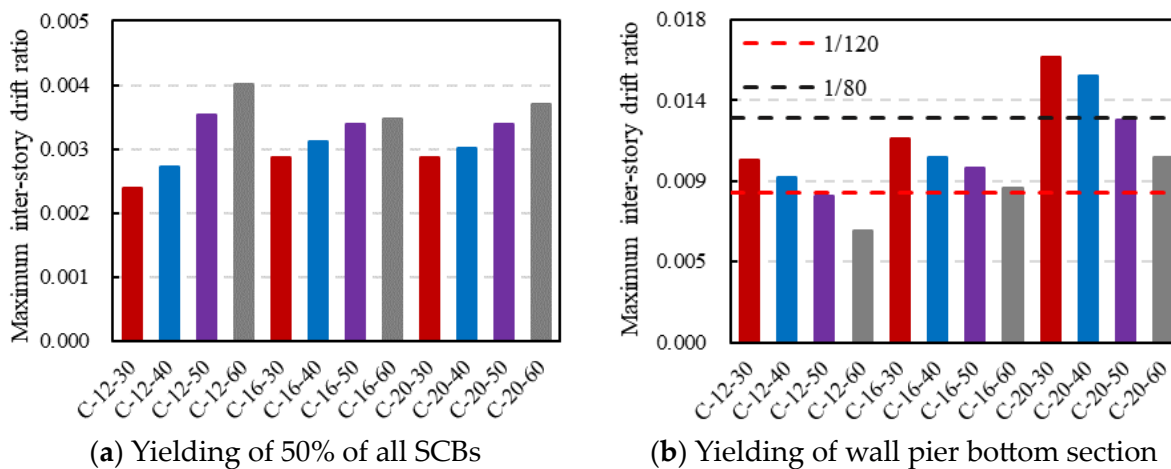
Figure 9. Maximum inter-story drift ratio corresponding to characteristic events.

5.2. Distribution Proportion of Bending Moment

The bending moment demands between the adjacent wall piers in the coupled SPRC walls is not evenly distributed. According to the analysis results, all the three prototype groups exhibit a similar moment distribution pattern, which can be demonstrated with the C-16 prototype cases as an example. As shown in Figure 10, when the maximum inter-story drift ratios are less than 0.0015, the bending moments resisted by the two wall piers are approximately equal. However, along with the increase in the maximum inter-story drift ratios, the difference in the bending moments developed in the compression and tension wall piers increases. The larger the CR, the greater the bending moment difference between the two wall piers.

(**a**) C-16-30

(**b**) C-16-40

(**c**) C-16-50

(**d**) C-16-60
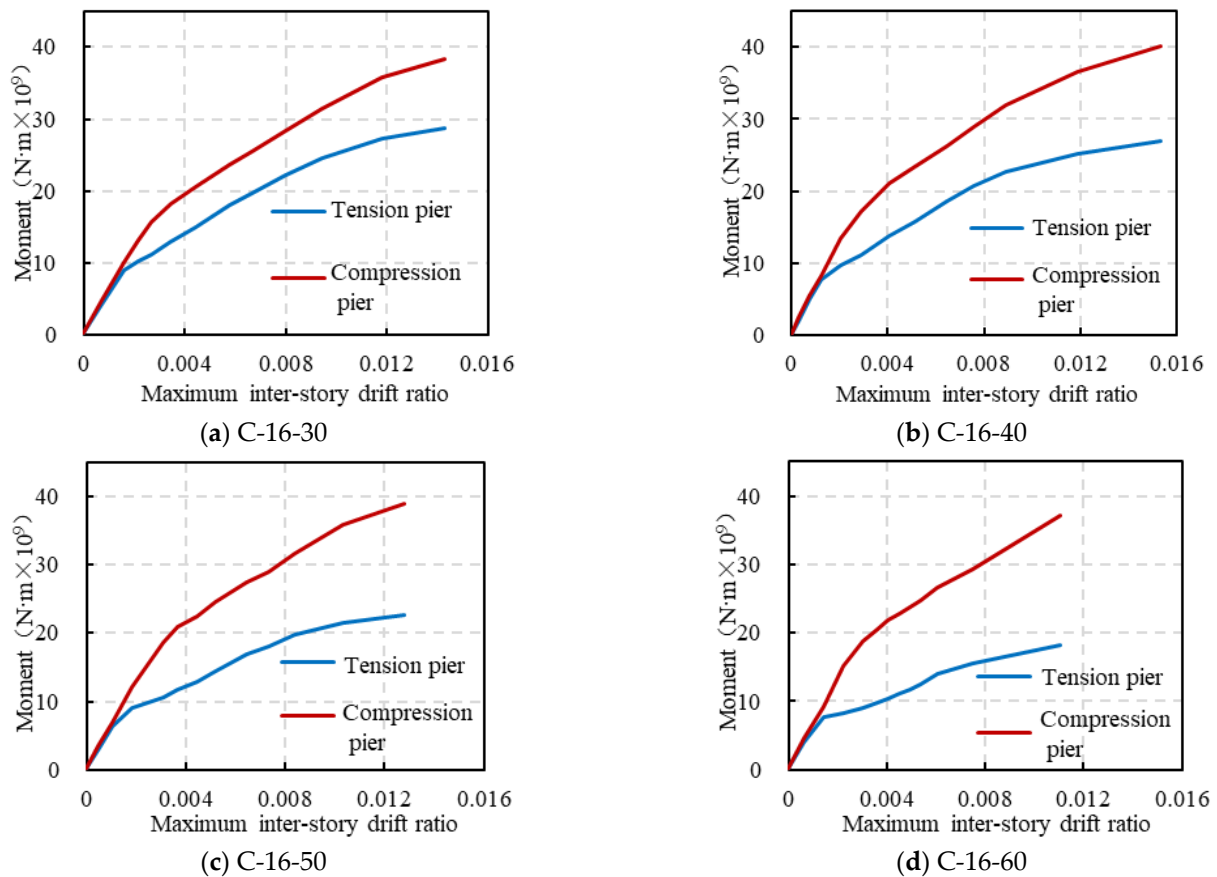
Figure 10. Moment distribution between wall piers of C-16 prototype cases.

The distribution proportions of bending moments between wall piers for all twelve prototype cases obtained from the analysis are compared with the proportions used in the design in Table 7. It can be seen that when the CR is 30%, 40% and 50%, the bending moment distribution proportions obtained from the pushover analysis are in good agreement with those used in the design. When the CR is 60%, the results of the pushover analysis are slightly different from those of the design. It is proved that the bending moment distribution proportions for the compression and tension wall piers provided in Table 2 are reasonable.

Table 7. Distribution of bending moments between wall piers.

ID	Pushover		Design	
	Tension Wall	**Compression Wall**	**Tension Wall**	**Compression Wall**
C-12-30	0.44	0.56		
C-16-30	0.44	0.56	0.45	0.55
C-20-30	0.44	0.56		
C-12-40	0.42	0.58		
C-16-40	0.42	0.58	0.42	0.58
C-20-40	0.42	0.58		
C-12-50	0.38	0.62		
C-16-50	0.39	0.61	0.39	0.61
C-20-50	0.39	0.61		
C-12-60	0.33	0.67		
C-16-60	0.34	0.66	0.36	0.64
C-20-60	0.35	0.65		

6. Dynamic Response Analysis

6.1. Earthquake Records

Five suitable earthquake ground motion records from the PEER Ground Motion Database and two software-generated artificial records were selected for the nonlinear dynamic analysis of the twelve prototype cases of the coupled SPRC composite walls. The basic information of the ground motion records is displayed in Table 8. Considering the site characteristics and the epicentral distance, the selected suite of ground motions is random and needs to be scaled to different PGA levels to create the moderate and rare earthquake input in accordance with the design level PGA of 0.4 g. The response spectra for the seven selected records scaled to a PGA of 0.4 g, and the target spectrum generated according to the Chinese code [15] are shown in Figure 11a. To further validate the applicability of the selected ground motion records, the difference between the average response spectrum of the selected suite of ground motion records and the code-generated design response spectrum should not exceed 10% at the two frequency domains of [0.1 s, T_g] and [$T_1 - 0.2$, $T_1 + 0.5$]. T_g and T_1 are the characteristic periods relating to the site and the fundamental period of the structural system respectively. The target design response spectrum is compared with the average response spectrum of the seven ground motion records, as shown in Figure 11b. It is clear that the selected suite of seven ground motion records can be used for the nonlinear dynamic analysis of the prototype cases.

Table 8. Selected suite of ground motion records.

ID	Magnitude	PGA (cm/s^2)	Duration (s)	Earthquake	Station
RSN951	6.7	99.47	34.99	Northbridge-01	Bell Gardens-Jaboneria
RSN1000	6.7	100.84	40	Northbridge-01	LA-Pico and Sentous
RSN1008	6.7	96.89	39.99	Northbridge-01	LA-W15th St
RSN5776	6.9	152.68	60	Iwate_Japan	Kami_Miyagi Miyazaki City
RSN5779	6.9	70.46	60	Iwate_Japan	Sanbongi Osaki City
Artificial 1 (R1)	-	44	30	-	-
Artificial 2 (R2)	-	44	30	-	-

6.2. Maximum Inter-Story Drift Ratio

Figures 12 and 13 show the average maximum inter-story drift ratios of the 12 coupled SPRC prototype structures under moderate and rare earthquake levels, respectively. The dashed vertical line in Figure 12, corresponding to the horizontal axis coordinate 1/120, represents the target maximum inter-story drift ratio under moderate earthquake levels. It is clear that none the 12 prototype cases exceed this limit. As can be seen in Figure 13, the maximum inter-story drift ratios of all prototype cases do not exceed the corresponding limit value of 1/80. By comparison of the overall distribution characteristics of the maximum inter-story drift ratios, it becomes clear that with the increase in the structural height, the influence of the CR increases. For example, in Figure 12c, the maximum inter-story drift ratios of the lower to middle stories of C-20-60 are larger than those of C-20–30, while those of the upper stories are vice versa. This means for the 20-story prototype cases, using high CR values can more efficiently control the inter-story drift ratios than using low CR values.
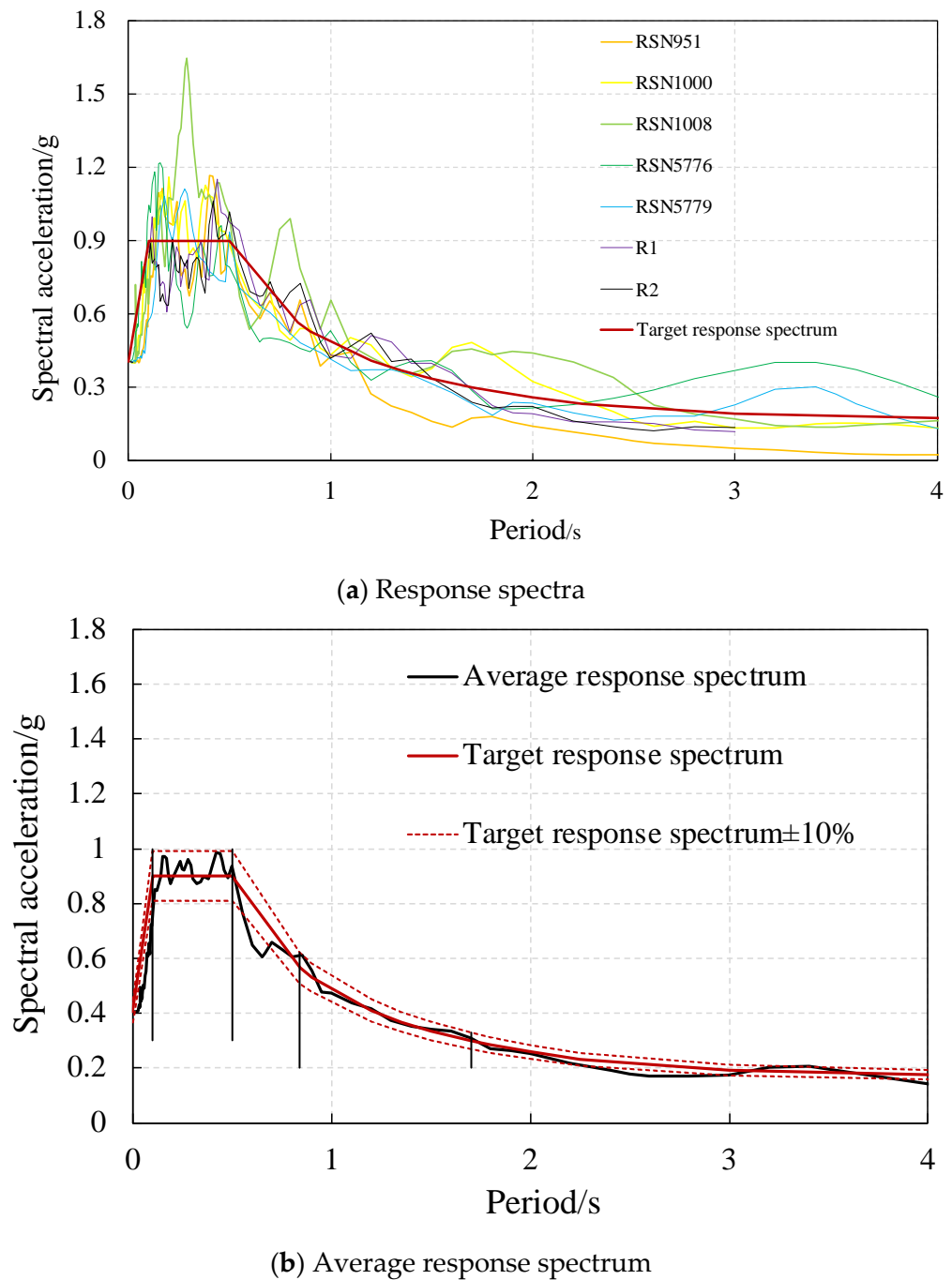
(**a**) Response spectra

(**b**) Average response spectrum

Figure 11. Response spectra of selected suite of ground motion records.

6.3. Story Shear Distribution

Figures 14–16 summarize the maximum story shear distribution of all the 12 prototype structures under moderate earthquakes. At the design stage, the story shear is evaluated based on the shear distribution factor β_i, as described in Section 2.1. It is shown from Figures 14–16 that, in general, the design maximum story shear distribution agrees well with the average analytical results for the upper stories. For the middle stories, the average analytical results are much lower than the design shear forces. For the lower stories, the design shear force is less than the average analytical shear force. However, it is also noticed that for each group of cases, the higher the CR, the smaller the difference between the design story shear and the average analytical story shear at the middle and upper stories, which is especially the case for the C-20 group cases.
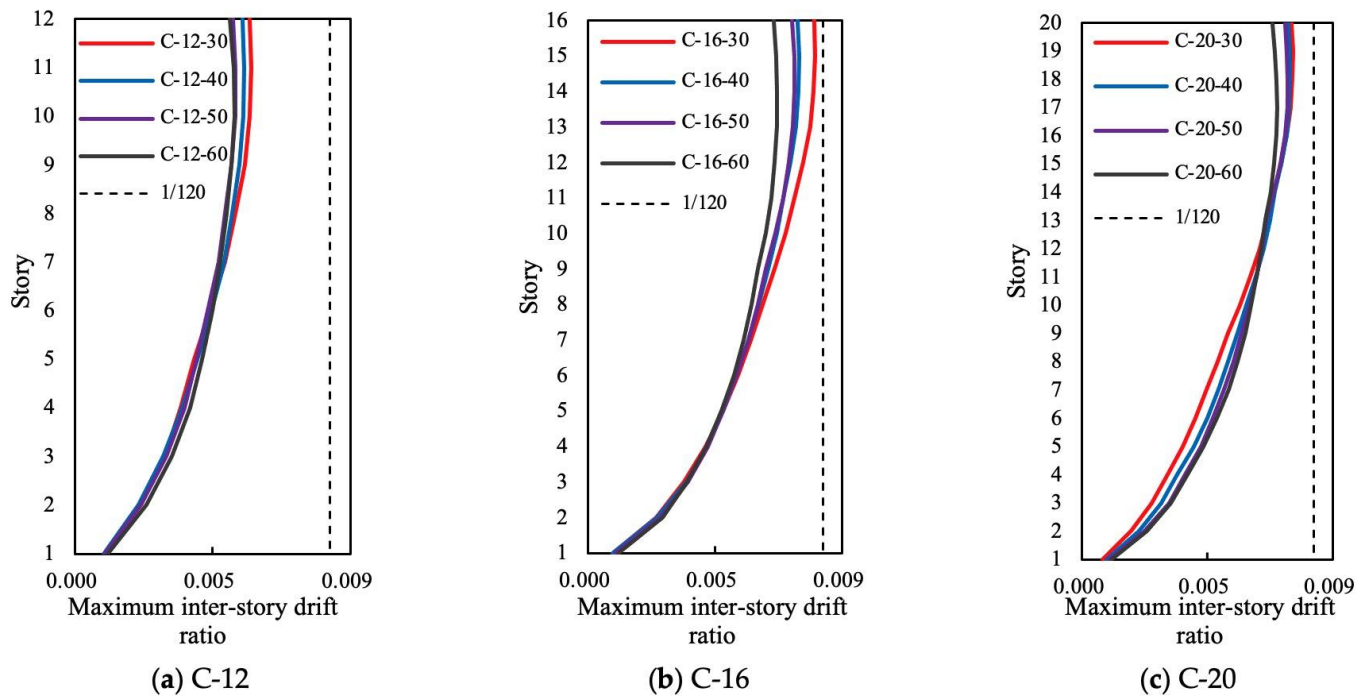
Figure 12. Average maximum inter-story drift ratios under moderate earthquakes.
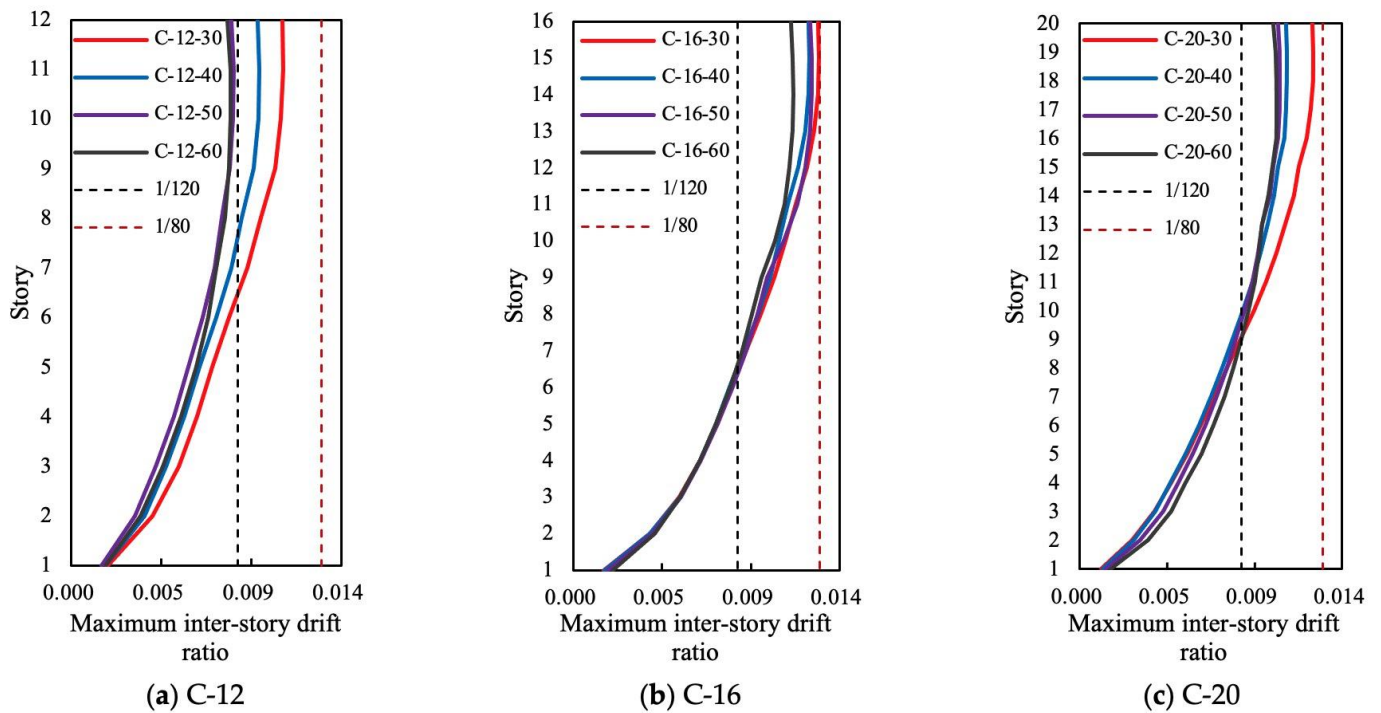
Figure 13. Average maximum inter-story drift ratios under rare earthquakes.
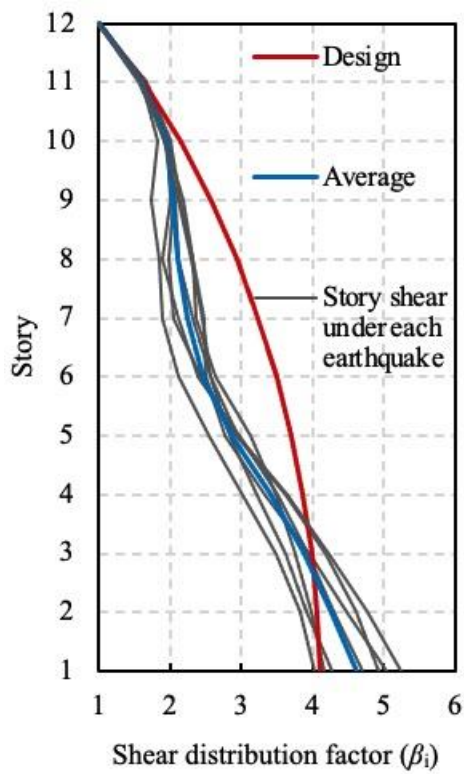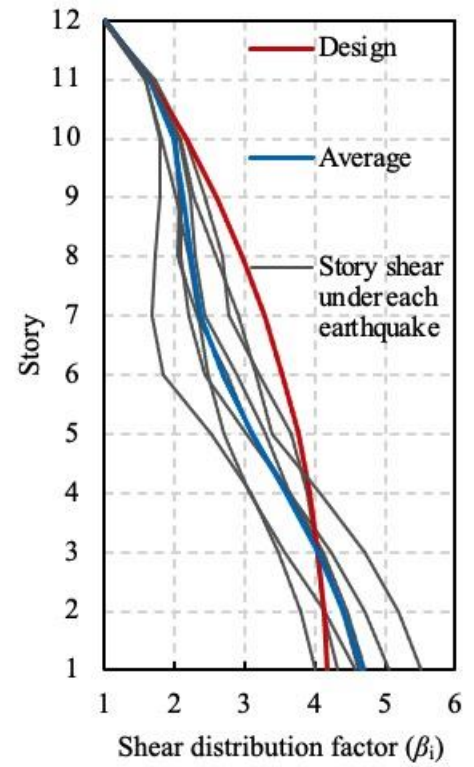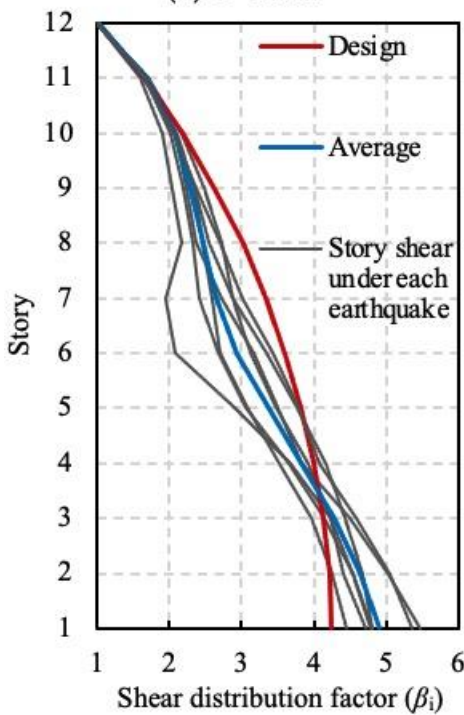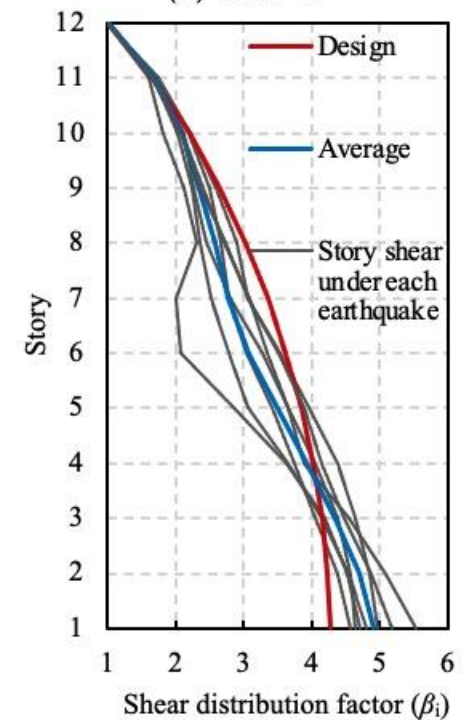
Figure 14. Story shear distributions of C-12 group under moderate earthquakes.
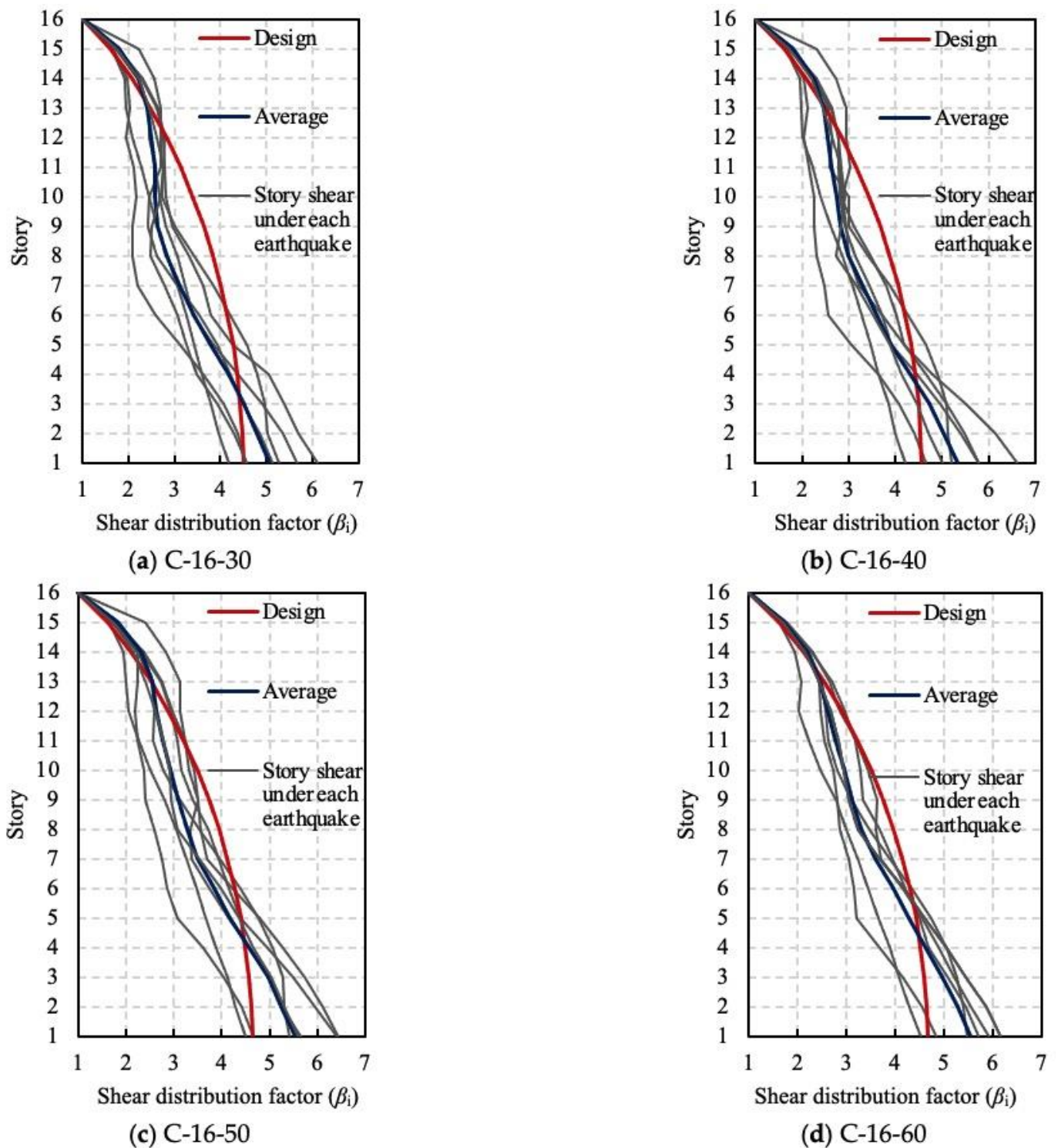
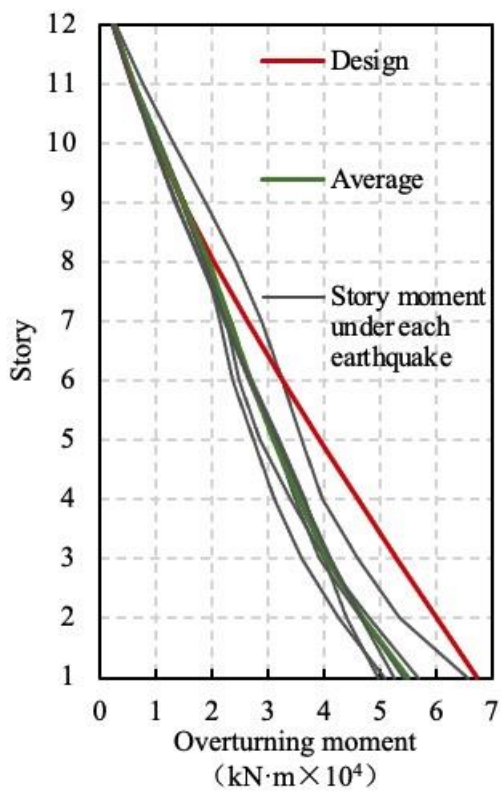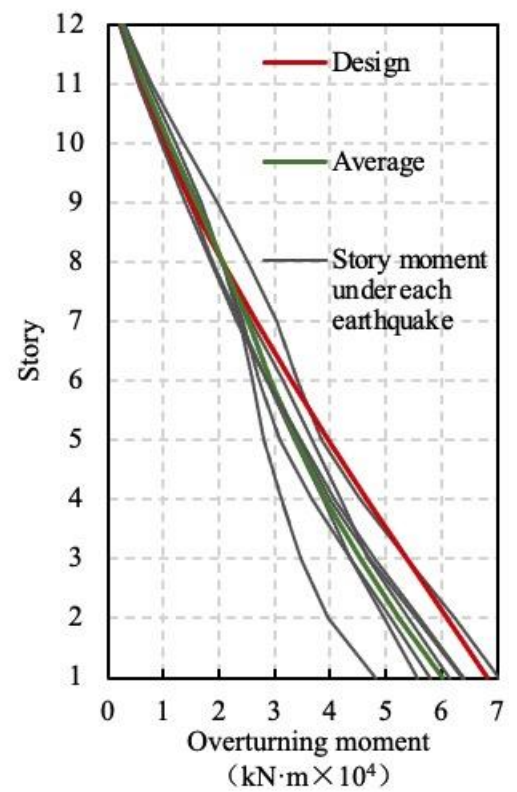**Figure 15.** Story shear distributions of C-16 group under moderate earthquakes.
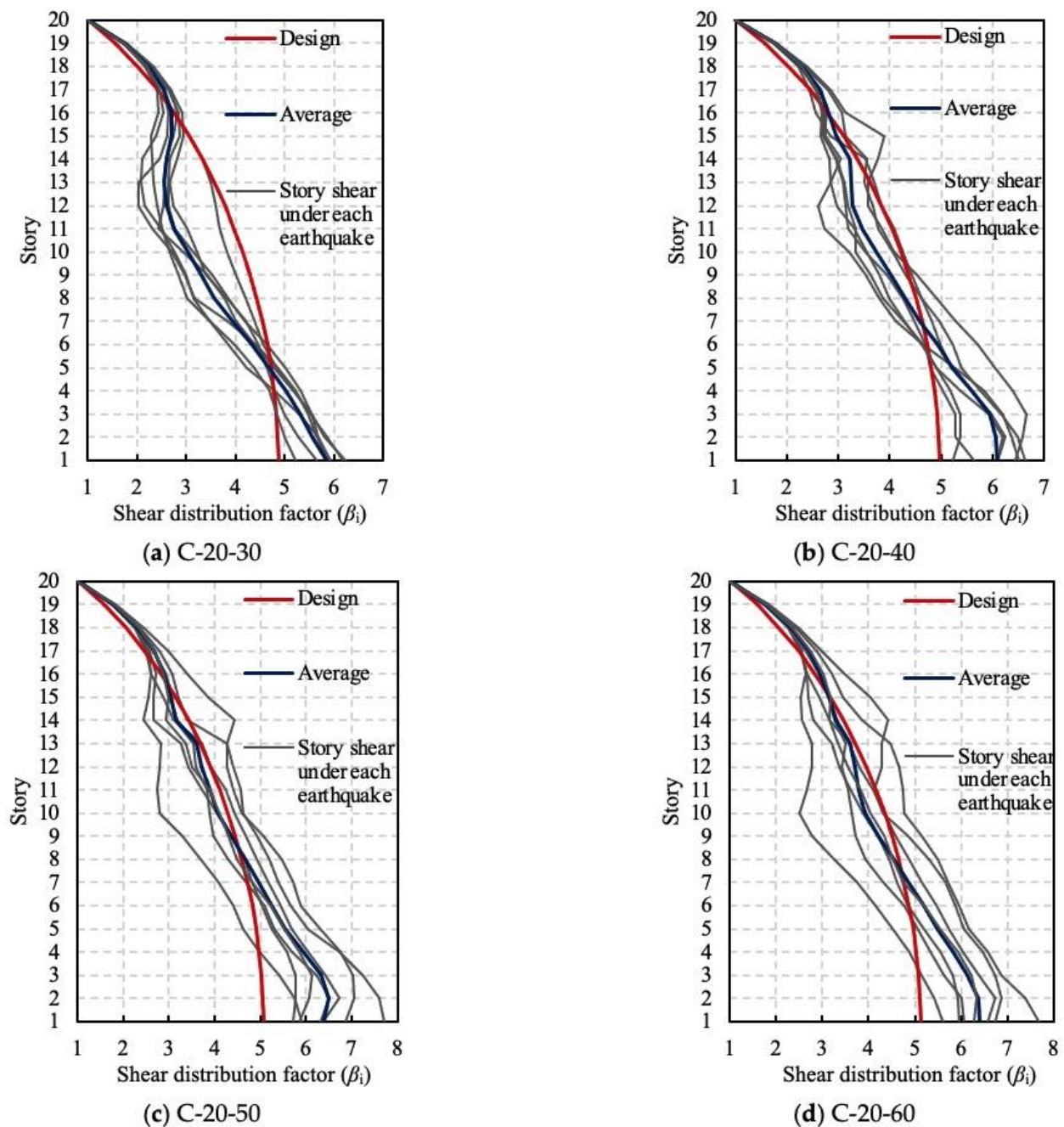
Figure 16. Story shear distributions of C-20 group under moderate earthquakes.
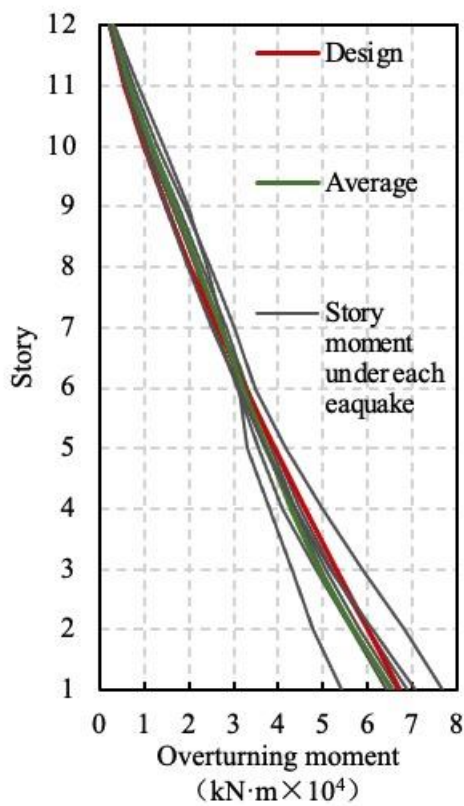
6.4. Overturning Moment Distribution

The analysis results for overturning moment distribution along the structural height of all 12 prototype structures under moderate earthquakes are shown in Figures 17–19. It can be seen from the figures that the CR values have a significant influence on the story bending moment distribution. When using CR values of 0.3 and 0.4, the design bending moment is only slightly smaller than the average analytical results at the upper stories of the structure, while the design bending moments in the middle and lower stories of the structure are greater than the average analytical overturning moments of the structure. When the CR values are 0.5 and 0.6, the design overturning moments are very close to the average analytical results.
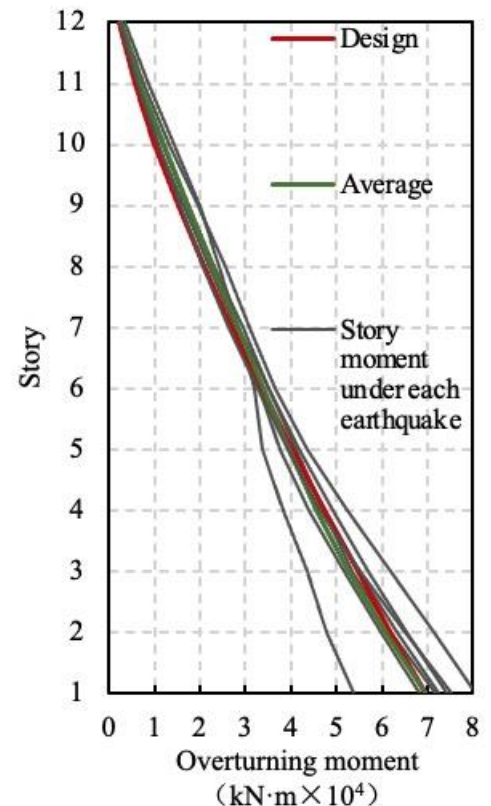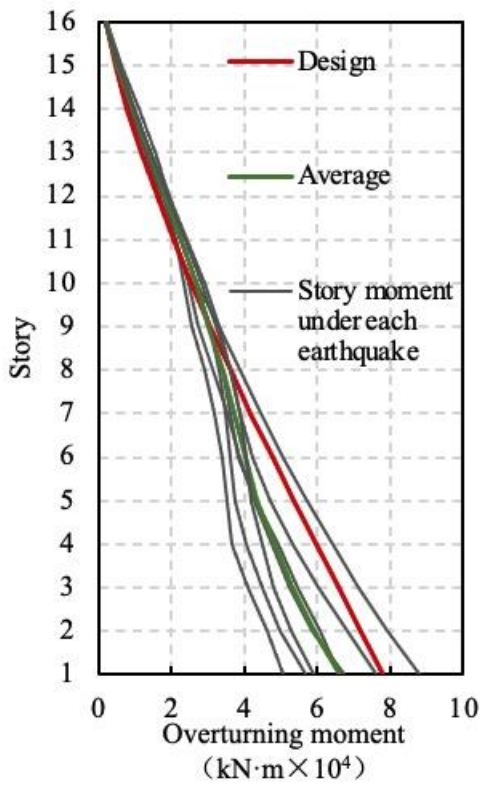
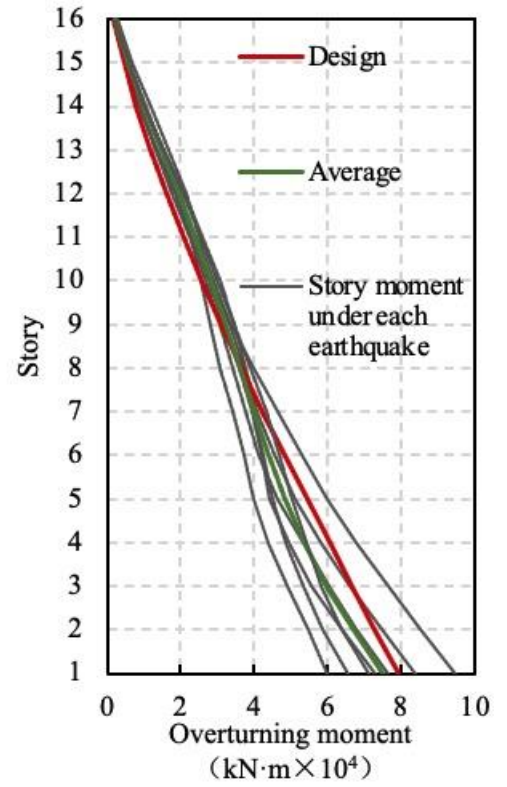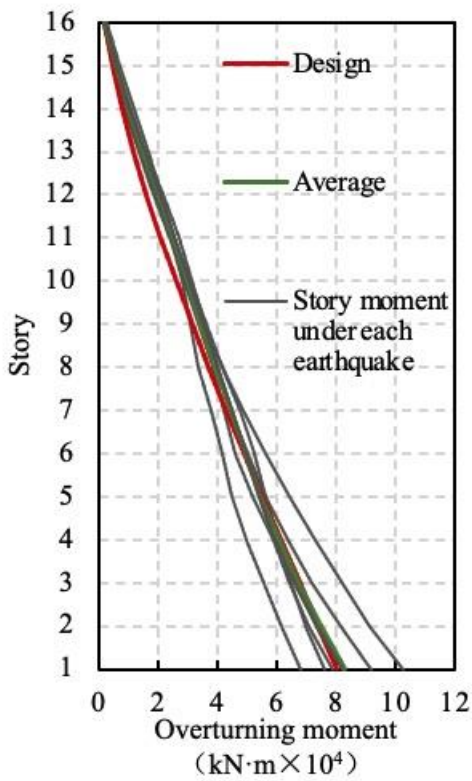**Figure 17.** Overturning moment distributions of C-12 group.
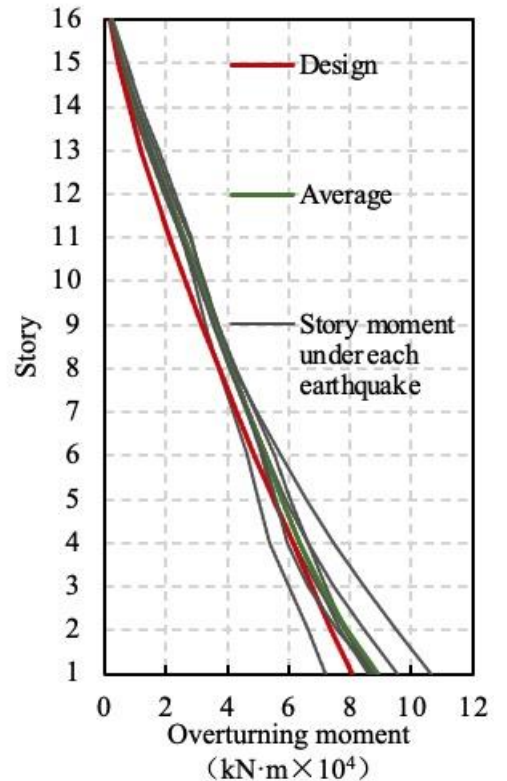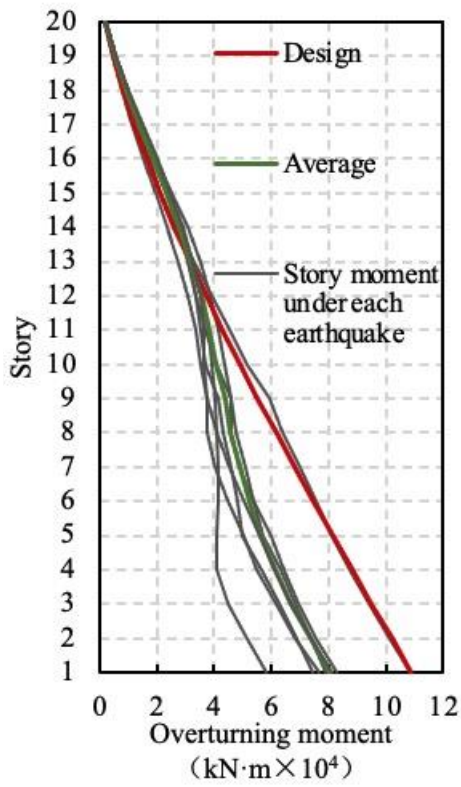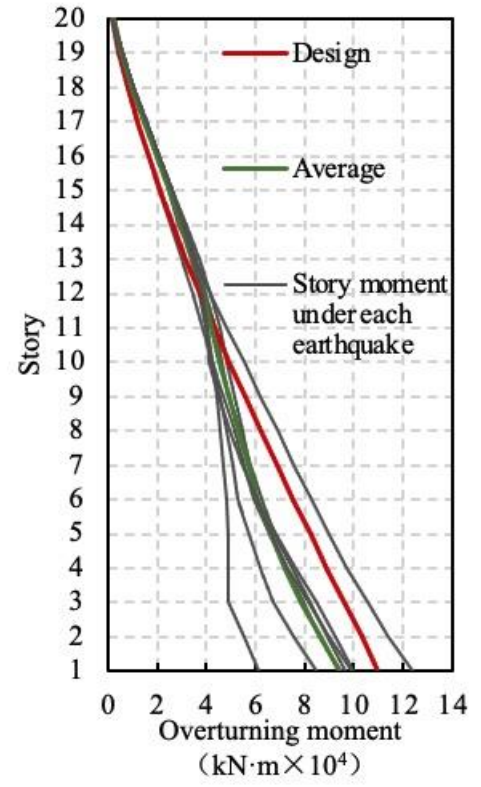
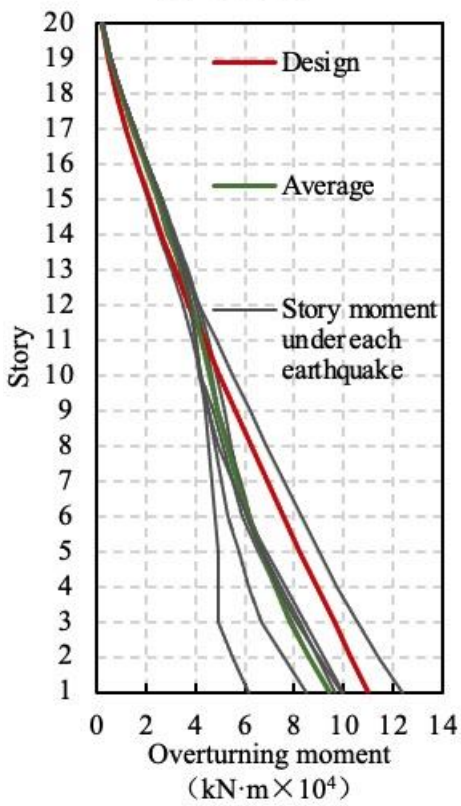(a) C-16-30

(b) C-16-40

(c) C-16-50

(d) C-16-60

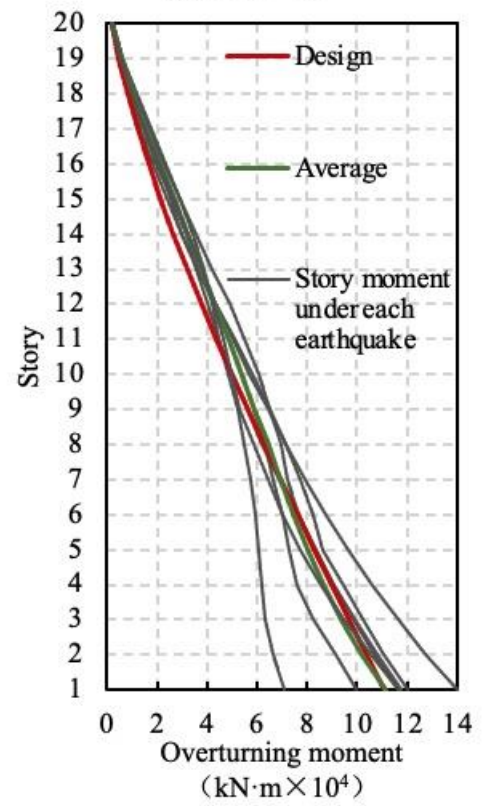**Figure 18.** Overturning moment distributions of C-16 group.

(a) C-20-30

(b) C-20-40

(c) C-20-50

(d) C-20-60

Figure 19. Overturning moment distributions of C-20 group.

7. Conclusions

In this research program, the EBPD method is developed for coupled SPRC composite wall systems and applied to the design of 12 prototype structures considering different story numbers and coupling ratios. The ABAQUS-based numerical techniques are applied to simulate the experiment on a 1:4 scale five-story coupled SPRC composite wall test model. The simulated results were found to agree very well with the experimental data and the accuracy of the numerical techniques was verified. Then, the 12 prototype cases of the coupled SPRC composite walls were modeled and numerically studied in a pushover analysis and nonlinear dynamic analysis. According to this study, the following conclusions can be drawn.

(1) The EBPD method is a very efficient seismic design method that combines the benefits and advantages of the energy balance concept and the plastic limit analysis. Through the application of the energy concept, the seismic design base shear can be directly obtained without the need for design iterations. The preferred plasticity development and distribution pattern can be directly reflected in the design stage. The pushover analysis and the nonlinear dynamic analysis prove the applicability and the efficacy of the EBPD method to the seismic design of coupled SPRC composite walls.

(2) The suggested numerical techniques with ABAQUS can be used to simulate the main seismic behavior of the coupled SPRC composite walls with good accuracy and efficiency.

(3) The pushover analysis results indicate that the yielding of the majority of the SCBs is the threshold of the yielding of the entire structural system. The greater the CR, the larger the roof lateral drift ratio corresponding to the yielding of the majority of the SCBs, and the smaller the roof lateral drift ratio corresponding to the yielding of the wall piers. The post-yield deformation capacity of the coupled SPRC wall system decreases with increases in the CR. However, the peak lateral load capacity increases with the CR. The limits of the maximum inter-story drift ratio corresponding to the yielding of SCBs and the bottom section of wall piers can be satisfied. The bending moment distribution pattern between the compression and tension wall piers agrees well with the design assumptions.

(4) The nonlinear dynamic analysis results indicate that the average maximum inter-story drift ratios can still be within the code limits under moderate and rare earthquakes. The average story shear distribution patterns show noticeable differences from the design story shear distribution assumption, but the design story forces tend to be safer compared with the numerical analysis results. Increasing the CR can reduce the difference between the design story shear and the average analytical story shear force. A similar trend is found in terms of the overturning moment distribution pattern between the two wall piers.

(5) The results of the pushover analysis and the dynamic response history analysis indicate that the influence of CR on the structural deformation responses is relevant to the structural height. For 12-story coupled SPRC composite walls, the suggested range of the CR is 30–40%; for 16-story and 20-story coupled SPRC composite walls, the suggested range of the CR is 50–60%.

Nomenclature

θ_u	target ultimate lateral drift ratio
θ_y	inter-story-drift ratio at yielding
θ_p	plastic rotation
γ	energy modification factor
μ	displacement ductility factor
λ_i	lateral force distribution factor for the ith floor
R_μ	ductility reduction factor
η	energy reduction factor
α	ratio of the initial stiffness to that after yielding
β_i	story shear distribution factor for the ith story
$\varepsilon_{c,e0}, \sigma_{c,e}$	concrete compressive strain and stress of elastic limit
$\varepsilon_{t,0}, f_t$	ultimate tensile strain and stress
$\varepsilon_{cu}, \sigma_{cu}$	ultimate compressive strain and stress of concrete
ε_{tu}	ultimate tensile strain of concrete
$f_c, \varepsilon_{c,0}$	concrete compressive strength and corresponding strain
ε_c, σ_c	concrete strain and stress during the hardening stage of compression
σ_t, ε_t	concrete stress at the hardening stage of tension and corresponding strain
$\varepsilon_{t,in}, \varepsilon_{c,in}$	cracking strain in the tensile stage and inelastic strain in the compression stage
$\varepsilon_{t,p}, \varepsilon_{c,p}$	tension plastic strain and compression plastic strain
ε_p	proportional limit stain of steel
ε_s	strain hardening ultimate strain of steel
ε_y	maximum yield strain of steel
ε_t	strength degradation strain of steel
ε_u	ultimate strain of steel
f_{b0}/f_{c0}	ratio of the biaxial compressive strength to the uniaxial compressive strength
m_i, k_i	concentrated mass and the lateral stiffness of the ith story
d	section depth of steel member
t_f	flange thickness
t_w	web thickness
b_f	flange width
M_i, K_i	the ith modal mass and stiffness
M_i *	ith effective modal mass
$S_{v,i}, S_{a,i}$	ith pseudo velocity, ith pseudo acceleration
N	total story number
K	ratio of second stress invariant on tensile meridian to that on compressive meridian
D_t, D_c	tensile and compressive damage variables
E_0	initial elasticity modulus
E_e, E_p	elastic and plastic energy of structure
E_I	input earthquake energy
V_y, Δ_y	design base shear and the corresponding roof lateral displacement
M, G	total mass and the seismic weight of the structure
G_i, G_n	seismic weight concentrated at ith floor and roof
M_{otm}, M_w	total overturning moment, overturning moment resisted by wall piers
M_{cw}, M_{tw}	overturning moment resisted by compression and tension piers
CR	coupling ratio
T	accumulated axial force transferred from all steel coupling beams
T_1, T_i	fundamental period of structure and period of ith mode
T_g	characteristic periods relating to the site
T_{eff}	equivalent fundamental period of structure
V_{bi}	shear demand of coupling beam at ith floor
V_{bmax}	maximum shear demand of coupling beam
V_n	shear strength of coupling beam after amplitude modification
F_i, h_i	lateral force at ith floor and structural height measured from ground to ith floor
ΔF_i	additional lateral force due to secondary effect
l_w	centroidal distance between two adjacent wall piers
f_y, f_u	yield and ultimate tensile stress of the steel

References

1. Broberg, M.; Shafaei, S.; Kizilarslan, E.; Seo, J.; Varma, A.H.; Bruneau, M.; Klemencic, R. Capacity Design of Coupled Composite Plate Shear Wall- Concrete-Filled System. *J. Struct. Eng.* **2022**, *148*, 04022022. [CrossRef]
2. Ma, Z.; Wu, Y.; Zhang, J.; Zhang, M. Experimental Study on Seismic Behavior of Coupled Steel Plate and Reinforced Concrete Composite Wall. *Buildings* **2022**, *12*, 2036. [CrossRef]
3. Dong, H.; Wu, Y.; Zhang, M.; Ma, Z. Seismic Behavior of Coupled Steel Plate and Concrete Composite Wall System. *Int. J. Civ. Eng.* **2023**, *21*, 1237–1256. [CrossRef]
4. Wu, Y.; Zhou, Q.; Su, Y.; Wang, B. Seismic Design Method and Experimental Study of Composite Steel Plate-Concrete Coupled Shear Wall Systems. *J. Build. Struct.* **2017**, *38*, 58–65. [CrossRef]
5. Wang, B.; Jiang, H.; Lu, X. Experimental and Numerical Investigations on Seismic Behavior of Steel Truss Reinforced Concrete Core Walls. *Eng. Struct.* **2017**, *140*, 164–176. [CrossRef]
6. Uang, C.M.; Bertero, V.V. Evaluation of Seismic Energy in Structures. *Earthq. Eng. Struct. Dyn.* **1990**, *19*, 77–90. [CrossRef]
7. Leelataviwat, S.; Goel, S.C.; Stojadinovic, B. Toward Performance-based Seismic Design of Structures. *Earthq. Spectra* **1999**, *15*, 435–461. [CrossRef]
8. Leelataviwat, S.; Goel, S.C.; Stojadinovic, B. Energy-based Seismic Design of Structures Using Yield Mechanism and Target Drift. *J. Struct. Eng.* **2002**, *128*, 1046–1054. [CrossRef]
9. Chao, S.H.; Goel, S.C. A Seismic Design Method for Steel Concentric Braced Frames (CBF) for Enhanced Performance. In Proceedings of the 4th International Conference on Earthquake Engineering, Taipei, Taiwan, 12–13 October 2006.
10. Chan-Anan, W.; Leelataviwat, S.; Goel, S.C. Performance-based Plastic Design Method for Tall Hybrid Coupled Walls. *Struct. Des. Tall Spec. Build.* **2016**, *25*, 681–699. [CrossRef]
11. Bai, J.; Cheng, F.; Jin, S.; Ou, J. Assessing and Quantifying the Earthquake Response of Reinforced Concrete Buckling-restrained Brace Frame Structures. *Bull. Earthq. Eng.* **2019**, *17*, 3847–3871. [CrossRef]
12. Sun, G.; Wei, X.; Gu, Q.; Wang, Y. Performance-based Plastic Design of Composite Partially-restrained Steel Frame-Reinforced Concrete Infill Walls with Concealed Vertical Slits. *Bull. Earthq. Eng.* **2020**, *18*, 1445–1474. [CrossRef]
13. Bai, J.; Yang, T.Y.; Ou, J. Improved Performance-based Plastic Design for RC Moment Resisting Frames: Development and A Comparative Case Study. *Int. J. Struct. Stab. Dyn.* **2018**, *18*, 1850050. [CrossRef]
14. Zhang, B.; Wu, Y.; Zhou, Q.; Bai, J.; Yang, Y.B. Energy-balance Based Plastic Design and Analysis of Hybrid Coupled Wall System. *Structures* **2021**, *33*, 4096–4111. [CrossRef]
15. *GB50011*; Code for Seismic Design of Buildings. China Building Industry Press: Beijing, China, 2010. (In Chinese)
16. Park, R. Ductility Evaluation from Laboratory and Analytical Testing. In Proceedings of the 9th World Conference on Earthquakes Engineering, Tokyo, Japan, 2–9 August 1988.
17. Chao, S.H.; Goel, S.C.; Lee, S.S. A Seismic Design Lateral Force Distribution based on Inelastic State of Structures. *Earthq. Spectra* **2007**, *23*, 547–569. [CrossRef]
18. *CSA A23.3-14*; Design of Concrete Structures. Canadian Standards Association: Toronto, ON, Canada, 2014.
19. El-Tawil, S.; Fortney, P.; Harries, K.; Shahrooz, B.; Kurama, Y.; Hassan, M.; Tong, X. *Recommendations for Seismic Design of Hybrid Coupled Wall Systems*; ASCE: Reston, VA, USA, 2009.
20. *JGJ138*; Code for Design of Composite Structures. China Architecture & Building Press: Beijing, China, 2016. (In Chinese)
21. *EN 1993-1-2:2005*; EUROCODE 3: Design of Steel Structures—Part 1.2: General Rules-Structural Fire Design. European Committee for Standardization: Brussels, Belgium, 2005.
22. Zhang, S.; Xu, J.; Lai, T.; Yu, Y.; Xiong, W. Bond Stress Estimation of Profiled Steel-concrete in Steel Reinforced Concrete Composite Structures Using Ensemble Machine Learning Approaches. *Eng. Struct.* **2023**, *294*, 116725. [CrossRef]
23. Chen, W.; Xu, J.; Li, Z.; Huang, X.; Wu, Y. Load-carrying capacity of circular recycled aggregate concrete-filled steel tubular stub columns under axial compression: Reliability analysis and design factor calibration. *J. Build. Eng.* **2023**, *66*, 105935. [CrossRef]